Wang *et al. Energy Mater* 2024;4:400056
DOI: 10.20517/energymater.2023.133

Energy Materials

Article

Open Access

Check for updates

Highly crystalline covalent triazine frameworks modified separator for lithium metal batteries

Yun Wang, Ruixue Sun, Yi Chen, Xuyang Wang, Yufei Yang, Xiaoyan Wang, Hui Nie*, Xingping Zhou, Bien Tan*, Xiaolin Xie

Key Laboratory of Material Chemistry for Energy Conversion and Storage, Ministry of Education, School of Chemistry and Chemical Engineering, Huazhong University of Science and Technology, Wuhan 430074, Hubei, China.

***Correspondence to:** Dr. Hui Nie, Key Laboratory of Material Chemistry for Energy Conversion and Storage, Ministry of Education, School of Chemistry and Chemical Engineering, Huazhong University of Science and Technology, 1037 Luoyu Road, Hongshan District, Wuhan 430074, Hubei China. E-mail: huinie@hust.edu.cn; Dr. Bien Tan, Key Laboratory of Material Chemistry for Energy Conversion and Storage, Ministry of Education, School of Chemistry and Chemical Engineering, Huazhong University of Science and Technology, 1037 Luoyu Road, Hongshan District, Wuhan 430074, Hubei, China. E-mail: bien.tan@mail.hust.edu.cn

How to cite this article: Wang Y, Sun R, Chen Y, Wang X, Yang Y, Wang X, Nie H, Zhou X, Tan B, Xie X. Highly crystalline covalent triazine frameworks modified separator for lithium metal batteries. *Energy Mater* 2024;4:400056. https://dx.doi.org/10.20517/energymater.2023.133

Received: 29 Dec 2023 **First Decision:** 12 Apr 2024 **Revised:** 30 Apr 2024 **Accepted:** 22 May 2024 **Published:** 3 Jun 2024

Academic Editors: Jinqiang Zhang, Hong Xu **Copy Editor:** Fangyuan Liu **Production Editor:** Fangyuan Liu

Abstract

Covalent organic frameworks (COFs) that selectively enable lithium ions transport by their abundant sub-nano or nanosized pores and polar skeleton are considered as emerging coating materials for separators of lithium metal batteries. However, the COF-coated separators that combine high ionic conductivity with excellent lithium ions transference number (t_{Li^+}) are still challenging, as the coating layer may increase the transport resistance of ions through the separator due to the elongated pathway. Different from conventional strategies that always focus on developing COFs with distinct structural motifs, this work proposes a crystallinity engineering tactic to improve the ion transport behaviors and thus battery performance. Amorphous (AM-CTF) and highly crystalline covalent triazine frameworks (HC-CTF) were successfully synthesized, and the effect of crystallinity of CTFs on the electrochemical properties of the separators and the battery performance are fully studied. Compared to amorphous covalent triazine framework, HC-CTF features a more regular structure and higher surface area, which further improves the t_{Li^+} (0.60) and ionic conductivity (0.67 mS cm^{-1}) of the coated separators. The $LiFePO_4$/Li cells assembled with the HC-CTF-coated separator exhibit an ultralong lifespan and extremely high-capacity retention (45.4% at 1 C for 1,000 cycles). This work opens up a new strategy for designing high-performance separators of lithium batteries.

Keywords: Covalent triazine frameworks, COF-modified separator, crystallinity of COF, lithium metal batteries

INTRODUCTION

Benefiting from the high theoretical specific capacity (3,860 mAh g^{-1}, ten times that of graphite) and low redox potential (-3.04 V, *vs.* standard hydrogen electrode) of lithium metal anodes, lithium metal batteries (LMBs) are considered as one of the most promising high-energy-density secondary batteries[1-4]. Their main challenge is the irregular lithium metal plating during charging, forming lithium dendrites[5-7]. Generally, uncontrolled lithium dendrite growth leads to the corrosion of metallic lithium and the consumption of liquid electrolyte, resulting in a low Coulombic efficiency (CE) and poor cycling performance. Further, the lithium dendrite can penetrate the separator, causing a short circuit and explosion of the battery[8,9]. Its growth is rooted in the slow mass transport of lithium ions (Li^+). When the diffusion rate of Li^+ in the electrolyte is slower than that consumed during the electrochemical deposition process, concentration gradients are established, and lithium dendrites tend to grow[10]. Thus, accelerating Li^+ transport in the bulk electrolyte is the key to relaxing the concentration gradients and thus achieving homogeneous lithium deposition[11]. Unfortunately, Li^+ are usually surrounded by solvent molecules due to their small radius. The bulky solvated Li^+ have reduced mobility; meanwhile, they always transport more slowly than the anions in electrolytes, resulting in a low Li^+ transference number (t_{Li^+}) of 0.2-0.4[12]. Separators are a key component of LMBs. Their surface modification to regulate the transport behavior of ions in electrolytes proves to be an effective strategy to suppress lithium dendrite growth[13-16].

Among the various coating materials, such as inorganic nanoparticles[13,17,18] and polymers with ionic groups[19-21], covalent organic frameworks (COFs) are emerging porous materials with tunable nanoscale pores and tailorable skeletons. They usually contain light elements such as C, H, O, N, and B. Thanks to the nanosized pores and polar functional groups on the pore walls, COFs are expected to greatly promote the selective transport of Li^+ by size-confinement effect and electrostatic interactions[22-24]. In addition, their intrinsic insolubility in electrolyte makes them potential candidates for surface modification of separators[25-27]. However, due to the rapid reaction between monomers and the limited reversibility of polymerization reactions, amorphous or poorly crystalline COFs are usually generated. These amorphous COFs would lead to ion pathways with higher tortuosity due to random stacking, thereby resulting in slower ion mobility and lower diffusion flux[28,29]. In addition, partial of the active sites (polar functional groups) are buried due to the limited surface area. Therefore, constructing COFs with good Li^+ transport ability remains a huge challenge[30]. To solve this problem, studies have been devoted to the structural engineering of COFs to accelerate the transport of Li^+. Cao *et al.* propose a sulfonate-rich COF with strong electronegativity and large interlayer spacing, which exhibited t_{Li^+} of up to 0.88[31]. Shi *et al.* fabricate two-dimensional COF nanosheets with different functionalities to improve the battery performance[32]. Furthermore, exfoliating the bulk COF into nanosheets with few or single layers to expose more active sites can accelerate ion transport[33].

This work develops a crystallinity engineering strategy for shortened ion diffusion pathways and more accessible active sites in the COF-coated separator, improving ionic conductivity and t_{Li^+}. Covalent triazine frameworks (CTFs) are chosen due to their large number of ordered nanoscale channels constituted by periodically connected triazine groups and versatile synthesis methods[34,35]. Compared to other COFs with highly reversible covalent linkages such as boroxine, boronate esters, imine and others, the CTFs constructed by the stable triazine linkages exhibit excellent chemical and thermal stability[35]. Additionally, the rich nitrogen atoms in CTF skeletons are beneficial for improving the electrolyte wettability and desolvation of Li^+, enhancing Li^+ transport[36,37]. To investigate the effect of the crystallinity of CTFs on the electrochemical performance of modified separators, amorphous (AM-CTF) and highly crystalline CTFs (HC-CTF) were synthesized and blade coated on polyethylene (PE) separators. As shown in Scheme 1, an

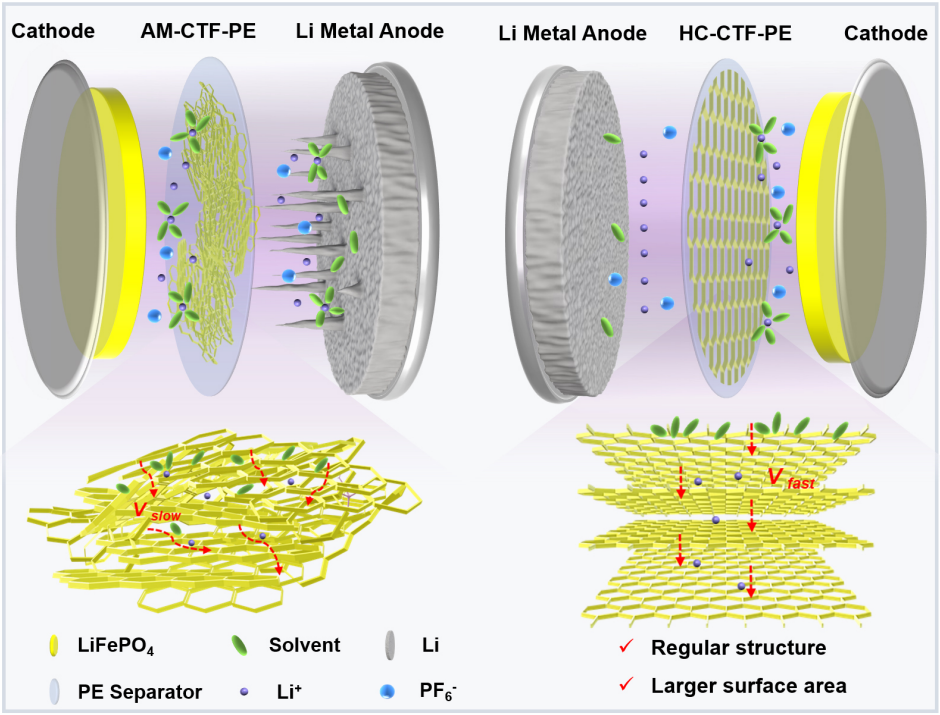

Scheme 1. Schematic illustration of the transport of ions in LMBs with AM-CTF-PE and HC-CTF-PE separators.

irregular stacking structure is formed in AM-CTF, which elongates the transport pathway and increases the transport resistance of ions through the separator. Meanwhile, the HC-CTF features a more regular structure and higher surface area, exposing more accessible active sites, which is conducive to faster selective transport of Li^+ and more uniform deposition. Compared to PE and AM-CTF-coated PE separators (AM-CTF-PE), the HC-CTF-coated PE separators (HC-CTF-PE) exhibit the highest t_{Li^+} of 0.6 and ionic conductivity of 0.67 mS cm^{-1}. Li//Li symmetric cells assembled with HC-CTF-PE separators deliver cycle stability over 300 h under a current density of 1 mA cm^{-2}. Capacity retention of 45.4% is achieved for $LiFePO_4$ (LFP)/Li cells with the HC-CTF-PE separators after 1,000 cycles at 1 C. This work opens up a new avenue to improve the performance of COF-coated separators for high-energy-density lithium batteries.

EXPERIMENTAL

Materials

All the materials were obtained from commercial sources and used as received without further purification. The 1-methyl-2-pyrrolidinone (NMP) was obtained from Sinopharm Chemical Reagent Co. (Shanghai, China). Commercial LFP cathode, polyvinylidene fluoride (PVDF, M_w ~1,000,000), LFP, and Super-P were from Canrd New Energy Technology Co. Ltd. (Guangdong, China). PE separators were received from Senior Technology Materials Co. Ltd. (Shenzhen, China). The liquid electrolyte (1 mol L^{-1} $LiPF_6$) in a mixed solvent of ethylene (EC) and dimethyl carbonate (DMC) with a volume ratio of 1:1 was from Duoduo Chemical Technology Co. Ltd. (Suzhou, China).

Preparation of CTF with different crystallinity

The AM-CTF was prepared through an amidine-based polycondensation method according to the reported literature. Furthermore, the HC-CTF was obtained by controlling the monomer feeding rate. The detailed

synthesis methods can be found in Supplementary Material. To uniformly disperse the CTF in the coating slurry, the prepared CTF was stored without vacuum drying.

Preparation of LFP cathode

First, 0.16 g PVDF, 0.16 g Super-P, and 1.28 g LFP were mixed and ground for 30 min; then, the mixed powders were dispersed in NMP with vigorous stirring for 5 h. The obtained slurry was spread on Al foil by blade coating and further dried at 60 °C. Finally, the cathode-coated Al foil was cut into discs with a diameter of 12 mm.

Preparation of CTF-PE separator

First, 5 mg PVDF was dispersed in NMP with vigorous stirring for ten minutes, and then 45 mg AM-CTF or HC-CTF (dry weight) was dispersed in NMP with ultrasound and stirring for 6 h. Next, the dispersed PVDF and CTF slurry was mixed with further stirring for 30 min. The obtained mixed slurry was coated on the surface of the PE separator using blades with thicknesses of 5, 10 and 20 μm, respectively. After drying at 60 °C for 12 h under vacuum, AM-CTF-PE and HC-CTF-PE separators with distinct thicknesses are obtained. Finally, the one-side coated separator was shaped as discs with a diameter of 19 mm.

Characterization

Fourier-transformed infrared (FT-IR) spectra were obtained by a Fourier-transformed infrared spectrometer (VERTEX 70). The structural information of CTFs was determined by powder X-ray diffraction (XRD, SmartLab-SE) with Cu-Kα radiation. Transmission electron microscopy (TEM) (Tecnai G2 20, FEI Holland) and field emission TEM (FE-TEM) (Talos F200, FEI Holland) were exploited to characterize the morphology of CTFs. The thermal stability of CTFs was characterized by a thermal gravimetric analysis (TGA) instrument (Perkin-Elmer Pyrisl) with a rate of 10 °C/min up to 800 °C under a nitrogen atmosphere. The Brunauer-Emmett-Teller (BET) specific surface area and pore size distribution were evaluated on ASAP2420-4MP at 77 K. Surface morphology and chemical composition of Cu electrodes, CTF powders, and different separators were analyzed using field emission scanning electron microscopy (FE-SEM, Nova NanoSEM 450). The element distribution is illustrated by energy-dispersive X-ray spectroscopy (EDS) mapping. To compare the wetting properties of various separators toward liquid electrolyte, the contact angles were tested using a contact angle tester (OCA20).

The electrolyte uptake (EU) was measured by immersing separators into the liquid electrolyte for one hour, and then the weight of separators was compared before and after absorbing. The electrolyte retention (ER) was evaluated by weighing the separators after they have absorbed the electrolyte and rested for a period of time.

$$EU(\%) = \frac{W_2\text{-}W_1}{W_1} \times 100\% \quad (1)$$

$$ER(\%) = \frac{W_3\text{-}W_1}{W_2\text{-}W_1} \times 100\% \quad (2)$$

Where W_1 is the weight of the original separators, and W_2 is the weight of the separators after absorbing the liquid electrolyte, and W_3 is the weight of the separator after it has absorbed the electrolyte and rested for a period of time.

The porosity was measured by weighing the separators before and after immersion in *n*-butanol:

$$Porosity = \frac{W_5\text{-}W_4}{V\times\rho}\times 100\% \quad (3)$$

where W_4 is the weight of original separators, and W_5 is the weight of separators after immersion in *n*-butanol, V represents the volume of separators, and ρ is the density of n-butanol (ρ = 0.81 g cm^{-3}).

Electrochemical measurements

CR2032 type coin cells were assembled to measure the electrochemical performance with different separators. LFP cathodes (12 mm), lithium metal (14 mm), and separators (19 mm) are used.

Electrochemical stabilization window

Electrolyte-soaked separator was sandwiched between lithium metal and stainless steel (SS) for linear sweep voltammetry (LSV) measurement on an AUTOLAB (PGSTAT302N). The scan rate is 10 mV s^{-1}.

Ionic conductivity (σ)

To calculate the ionic conductivity, electrochemical impedance spectroscopy (EIS) measurement was carried out:

$$\sigma = \frac{d}{R_d\times S} \quad (4)$$

where d is the thickness of the separator, S is the area of the separators, and R_d is the bulk ohmic resistance of the electrolyte.

Lithium ions transference number (t_{Li^+})

Combining chronoamperometry and EIS analysis with lithium symmetric cells, t_{Li^+} was evaluated by

$$t_{Li^+} = \frac{I_s(\Delta V\text{-}I_0R_{el}^0)}{I_0(\Delta V\text{-}I_sR_{el}^s)} \quad (5)$$

where I_0 is the initial current, I_s is the steady-state current, R_{el}^0 is the interfacial resistance before polarization, R_{el}^s is the interfacial resistance after polarization, and the constant step potential (ΔV) is 10 mV.

RESULTS AND DISCUSSION

CTFs were synthesized by a condensation reaction between 1,4-phthalaldehyde and terephthalamidine dihydrochloride, named CTF-HUST-1, according to reported procedures[38] [Figure 1A]. This one-pot polymerization was carried out at mild conditions (120 °C and ambient pressure at air atmosphere), which is beneficial for large-scale synthesis. By controlling the nucleation and crystal growth rates, the crystallinity of CTFs can be adjusted. When the monomers were fed in one step, the nucleation process is too fast and AM-CTFs are formed. By tuning the feeding rate of 1,4-phthalaldehyde (30 μL min^{-1}), slow nucleation was achieved and CTFs with high crystallinity were generated[39]. The successful formation of the triazine

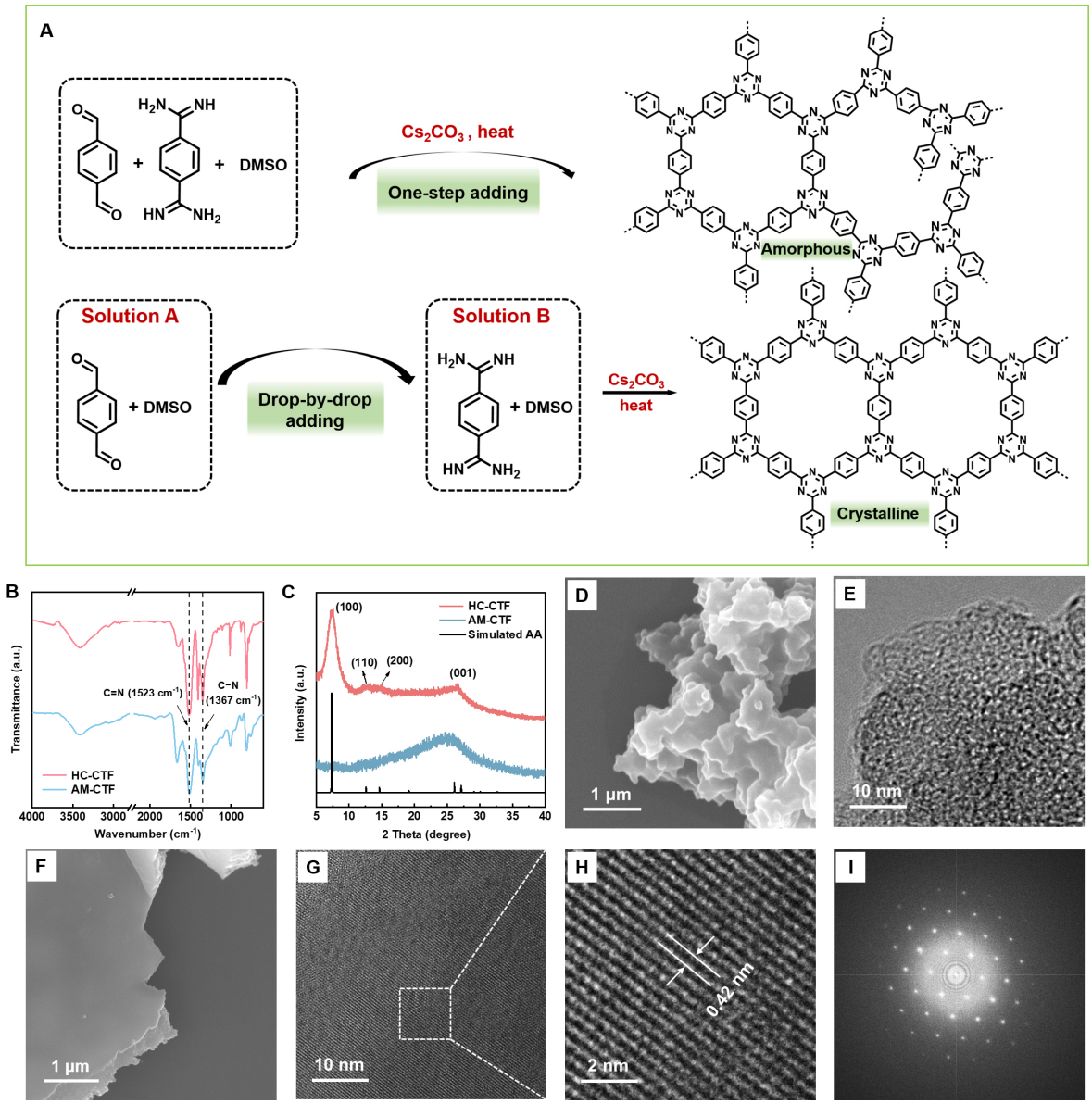

Figure 1. (A) Schematic synthesis of AM-CTF and HC-CTF; (B) FT-IR spectra; (C) PXRD patterns of AM-CTF and HC-CTF; (D) FE-SEM image and (E) FE-TEM image of AM-CTF; (F) FE-SEM image; (G)FE-TEM image and (H) high-magnification FE-TEM image of HC-CTF; (I) FFT image from the area of interest in (G).

frameworks was illustrated by FT-IR spectra. As shown in Figure 1B, the characteristic vibrations of the triazine units appear at 1,523 cm^{-1} (C=N) and 1,367 cm^{-1} (C-N) for both AM-CTF and HC-CTF, which is accordant with that in the literature[38]. The structures of AM-CTF and HC-CTF were characterized by solid-state cross-polarization magic angle spinning carbon-13 nuclear magnetic resonance (CP-MAS ^{13}C NMR), as shown in Supplementary Figure 1. The results demonstrate that there is essentially no difference between the two structures in solid-state CP-MAS ^{13}C NMR spectroscopy. The peaks with chemical shifts at 128 and 138 ppm are attributed to the phenyl carbons, while the peak with chemical shift at 179 ppm is attributed to the carbon in the triazine ring. Powder X-ray diffraction (PXRD) was used to analyze the structural differences between AM-CTF and HC-CTF [Figure 1C]. The PXRD pattern of AM-CTF shows a broad peak at 25.88°, indicating no long-range crystalline order. For the HC-CTF, diffraction peaks at about

7.4°, 12.7°, 14.7° and 26.2° are observed. According to literature, these peaks can be assigned to (100), (110), (200), and (001) facets, respectively, indicating the AA stacking arrangement of crystalline HC-CTF[39].

To further study the CTF structures, FE-SEM, TEM, and FE-TEM were exploited to show their morphology and crystallinity. From FE-SEM, particles with no regular morphology are observed for AM-CTF [Figure 1D]. Meanwhile, the FE-TEM image of this sample shows no lattice fringes [Figure 1E]. Interestingly, as shown in Figure 1F and Supplementary Figure 2, particles with a much smoother surface and a more regular shape are observed for HC-CTF, compared to AM-CTF. FE-TEM images reveal their crystalline characteristic and clear lattice fringes with interplanar lattice spacing of 0.42 nm [Figure 1G and H]. The fast Fourier transform (FFT) pattern [Figure 1I] in Figure 1G illustrates the crystalline structure of the HC-CTF. The results show that CTFs with different crystallinity were successfully synthesized by tuning the feeding rate of reactants.

To evaluate the porosity of AM-CTF and HC-CTF, nitrogen adsorption-desorption isotherms were performed at 77 K [Figure 2A]. The isotherm sorption profile of HC-CTF shows the typical type I characteristics, suggesting the existence of a large number of micropores. Through the nonlocal density functional theory method, the pore size distribution of HC-CTF is close to the reported calculated theoretical values[39] [Figure 2B]. The surface area calculated by the BET model is 652.18 $m^2 g^{-1}$. However, the BET surface area of AM-CTF drops sharply to 55.01 $m^2 g^{-1}$. The regular and interconnected channels with pores can facilitate a large accessible surface area for nitrogen in the BET measurement. And this morphology is suitable for diffusion of ions. Meanwhile, insignificant microporous structures are observed, suggesting structural defects and a rough texture for AM-CTF [Figure 2B]. The TGA measurement [Figure 2C] reveals that AM-CTF and HC-CTF display outstanding thermal stability under nitrogen atmosphere, and up to 80% of their weight is retained at temperatures of up to 650 °C, implying the formation of a highly thermal stable triazine framework. Notably, AM-CTF shows a relatively slight weight loss around 250 °C, possibly due to the presence of some unreacted terminal aldehyde groups.

The AM-CTF and HC-CTF were exploited as building blocks for functional layers on commercial PE separators. CTF-modified separators were prepared using the blade coating [Supplementary Figure 3]. This versatile method enables large-scale fabrication of the coated separator [Supplementary Figure 4]. As shown in Supplementary Figure 5A and B, the PE separator has porous and fibrous morphology. For the AM-CTF-modified PE separator (AM-CTF-PE) and the HC-CTF-modified separator (HC-CTF-PE), the CTF particles are uniformly distributed on the surface of the PE separator [Figure 3A and B]; meanwhile, some inevitable voids are observed on the surface of AM-CTF-PE and HC-CTF-PE separators [Supplementary Figure 5C and D]. EDS mapping of N elements shows a uniform distribution of CTFs (inset of Figure 3A and B). Using the same slurry concentration and coating procedures (the distance from the blade to PE surface is 5 μm for the spreading of slurry), the AM-CTF-PE and HC-CTF-PE with a coating layer thickness of about 1.5 μm are obtained, as shown from the cross-sectional SEM images [Figure 3C and D]. In addition, except the vibration peaks of -CH_2- (2,915 and 2,846 cm^{-1}) for PE, the characteristic vibration peaks of the triazine units (1,523 and 1,367 cm^{-1}) can be observed in the FT-IR spectra for AM-CTF-PE and HC-CTF-PE separators [Supplementary Figure 6]. These results further confirm the coating of CTF on the PE separator surface. The photographs in Figure 3E exhibit that AM-CTF-PE and HC-CTF-PE separators are flexible enough to maintain their original shape under varying bending conditions. Besides, AM-CTF and HC-CTF layers are firmly attached to the PE separator through blade coating, as evidenced by no stripped and cracked yellow CTF-coated layers after repeated folding and unfolding [Figure 3F]. This property is extremely important for the cycling stability and safety of LMBs.

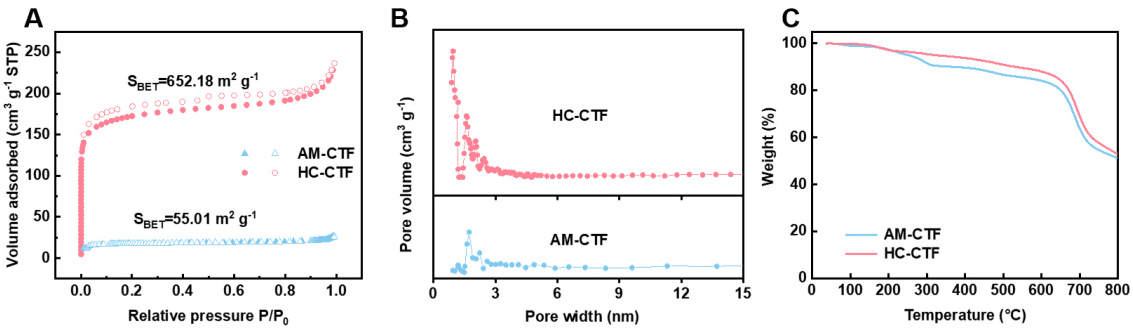

Figure 2. (A) N_2 adsorption and desorption isotherms; (B) Pore size distributions and (C) TGA curves of AM-CTF and HC-CTF.

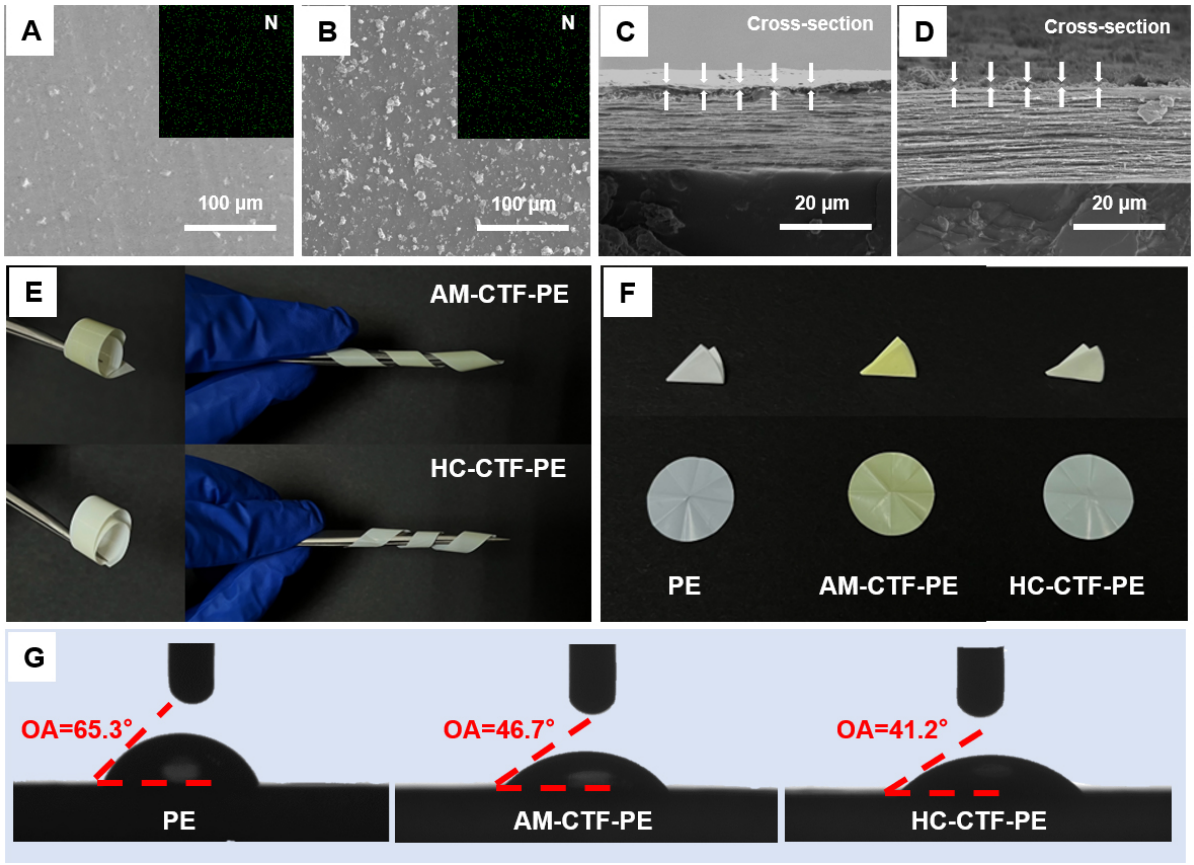

Figure 3. Top-view SEM images of (A) AM-CTF-PE and (B) HC-CTF-PE separators. Inset is the EDS mapping of N elements; Cross-sectional SEM images of (C) AM-CTF-PE and (D) HC-CTF-PE separators; (E)Photographs of AM-CTF-PE and HC-CTF-PE separators under bending conditions; (F) Photographs of PE, AM-CTF-PE and HC-CTF-PE separators after folding; (G) Contact angle images of PE, AM-CTF-PE and HC-CTF-PE after dropping liquid electrolyte on the surface.

Similar to the CTF samples, the BET surface area, pore volume and porosity of the HC-CTF-PE separators are higher than those of the AM-CTF-PE separator [Supplementary Table 1]. The electrolyte wettability of AM-CTF-PE and HC-CTF-PE separators is obviously improved compared with bare PE separators, with contact angles of 46.7°, 41.2° and 65.3°, respectively [Figure 3G]. This improved property of modified separators is mainly due to the CTF layer with nanosized pores and polar skeleton, which feature intrinsic affinity with polar electrolyte. Compared with AM-CTF-PE, the enhanced wettability of HC-CTF-PE

separators originates from their larger specific surface area and pore volume. Meanwhile, the EU and ER of the HC-CTF-PE separator are higher than those of the AM-CTF-PE separator [Figure 4A and B]. The well-connected porous structure of HC-CTF can facilitate the penetration and retention of electrolyte, which are beneficial for fast ion transport.

The electrochemical stability of separators is the basis for the battery safety. As shown in Supplementary Figure 7, the LSV curves show that AM-CTF-PE and HC-CTF-PE separators can stably operate at a voltage range of 2.5-3.9 V, suggesting that these separators are suitable for commonly used batteries. The ion transport behaviors of the CTF-modified separators were further studied using electrochemical measurements. The ionic conductivity of the separators was evaluated by EIS using assembled SS/separator/SS cells. The intersection of the EIS plot and the x-axis is extracted for the conductivity calculation of the separators [Figure 4C]. The calculated ionic conductivities of the HC-CTF-PE, AM-CTF-PE and PE separators are 0.66, 0.46 and 0.33 mS cm^{-1}, respectively [Supplementary Table 2]. The enhanced electrolyte wettability and larger specific surface area of the HC-CTF-PE separator may contribute to its promoted ion transport ability.

To evaluate the selective transport ability of Li^+ for different separators, the t_{Li^+}, representing the ratio of Li^+ mobility to total ionic mobility, was evaluated using the Bruce-Vincent method[40]. The chronoamperometry profiles of HC-CTF-PE and AM-CTF-PE assembled Li//Li symmetric cells are present in Figure 4D and E. And the potentiostatic polarization process was endowed from the initial to the steady state. From the EIS spectra (inset of Figure 4D and E, Supplementary Figure 8, Supplementary Table 3), the charge transfer resistance (R_{ct}) of the HC-CTF-PE separator is lower than that of AM-CTF-PE and PE separators both before and after polarization. Accordingly, the $t_{Li^+}$of HC-CTF-PE, AM-CTF-PE and PE separators are 0.6, 0.41 and 0.31, respectively. The schematic illustrations of ion transport process in PE, AM-CTF-PE and HC-CTF-PE separators are shown in Supplementary Figure 9. For bare PE separators, the Li^+ in electrolyte are always in bulky solvated form, which have reduced mobility compared with that of anions[41]. Thus, the t_{Li^+} of 0.31 is obtained [Supplementary Figure 8]. For CTF-coated PE separators, the abundant polar triazine units can enhance the affinity of the separator to electrolyte, and the rich polar N atoms with lone pair electrons in CTF layer may interact with the solvated Li^+ through electrostatic interaction[42,43], thus reducing the size of the solvated cluster and accelerate their transport[44]. More importantly, the HC-CTF, which features nanosized pores with the highest specific surface area and pore volume, provides more active sites and ion transport channels for efficient desolvation with sufficient interaction and the mostly enhanced transport of Li^+.

To further demonstrate the desolvation effect of CTF layers, the activation energy (E_a) of ion desolvation was evaluated using the Arrhenius equation. Based on temperature-dependent EIS measurements [Supplementary Figure 10], the semicircles of the Nyquist plot in the middle-high frequency region are denoted to the R_{ct}. According to Arrhenius equation, the E_a can be calculated by linear fitting of ln (R_{ct}^{-1}) *vs.* 1/T:

$$1/R_{ct} = A\exp(-E_a/RT),$$

where A, R, and T represent the frequency factor, ideal gas constant, and absolute temperature, respectively. After fitting, as shown in Figure 4F, the E_a values of HC-CTF-PE and AM-CTF-PE are 59.26 and 60.71 kJ mol^{-1}, respectively, which are lower than that of pristine PE (63.13 kJ mol^{-1}), confirming the

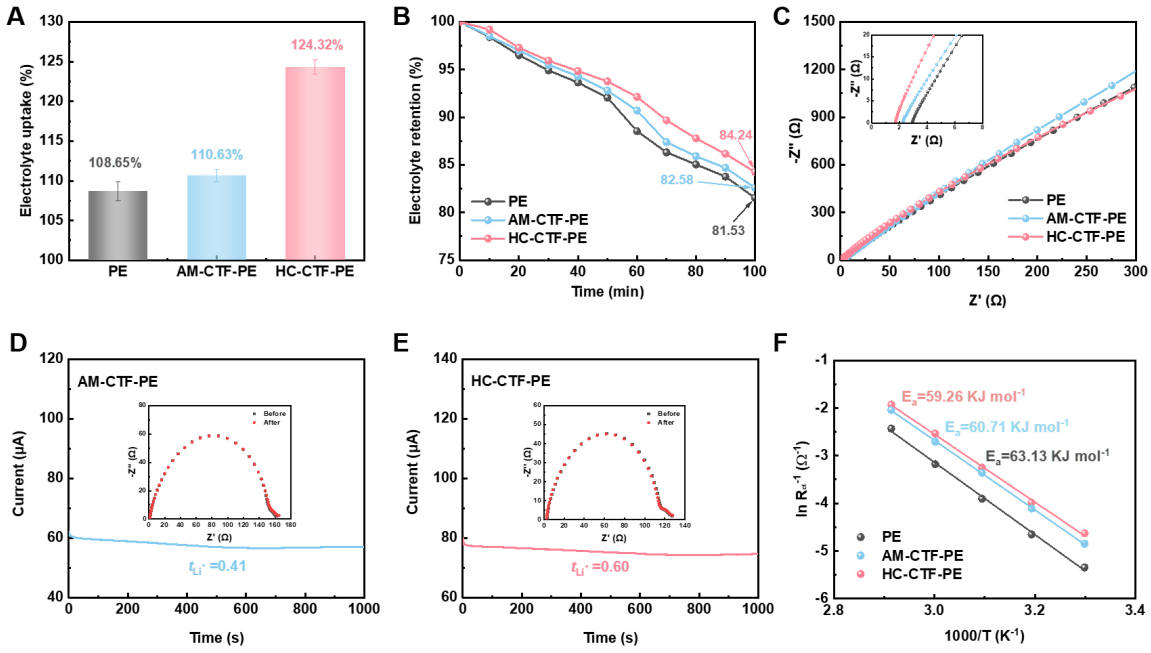

Figure 4. (A) Electrolyte uptake and (B) electrolyte retention of the PE, AM-CTF-PE and HC-CTF-PE separators; (C) EIS plots of the PE, AM-CTF-PE and HC-CTF-PE separators, the inset shows enlarged EIS plots in the high-frequency region; Chronoamperometry profiles of (D) AM-CTF-PE and (E) HC-CTF-PE separators. Inset of (D) is the AC impedance spectra before polarization, and inset of (E) is the AC impedance spectra after polarization; (F) Fitting and evaluation of activation energy using the Nyquist plots.

desolvation effect of CTF coating layers. Based on above results, the CTF coating improves both the t_{Li^+} and ionic conductivity of the PE separator. According to the Bruce-Vincent method and Sand's time model[45,46], it is expected that the HC-CTF separator with the highest t_{Li^+} and ionic conductivity can delay the lithium dendrite growth and is helpful for stable lithium deposition[47,48].

To investigate the lithium deposition behavior of CTF-modified separators, the long-term galvanostatic discharging and charging voltage profiles of Li//Li symmetric cells were measured. Figure 5A shows the performance of these cells with PE, AM-CTF and HC-CTF separators at a current density of 1 mA cm^{-2} and a fixed capacity of 1 mAh cm^{-2}. The overpotential of the symmetric cells assembled with PE separators gradually increases as early as 120 h and fluctuates dramatically afterward. This results from the rapid electrolyte consumption and lithium dendrite growth caused by side reactions and polarization phenomena in the cells. The overpotential of symmetric cells with CTF-coated separators is lower than that of PE separators. Moreover, the overpotential of AM-CTF-PE separators gradually increases at about 170 h, while that of HC-CTF-PE separators is stable up to 300 h. From the voltage-time curves at different cycling times [Supplementary Figure 11], it is observed that the Li//Li symmetric cells assembled with HC-CTF-PE separators have the lowest overpotential, followed by AM-CTF-PE separators, while the highest is the PE separator. A higher overpotential suggests a larger nucleation energy barrier for the deposition of metallic lithium. According to literature, it may induce the dendritic lithium growth during plating[49]. Further, at a current density of 2 mA cm^{-2} and capacity of 2 mAh cm^{-2}, the Li//Li symmetric cells assembled with HC-CTF-PE separators show better cycling stability and lower overpotential. [Supplementary Figure 12]. These results suggest that the CTF layer effectively delays the growth of lithium dendrite. To further study the dendrite suppressing effect of HC-CTF-PE separators, the morphology of the lithium plating onto Cu foils with various separators at a current density of 0.5 mA cm^{-2} were monitored. As shown in Figure 5B-D,

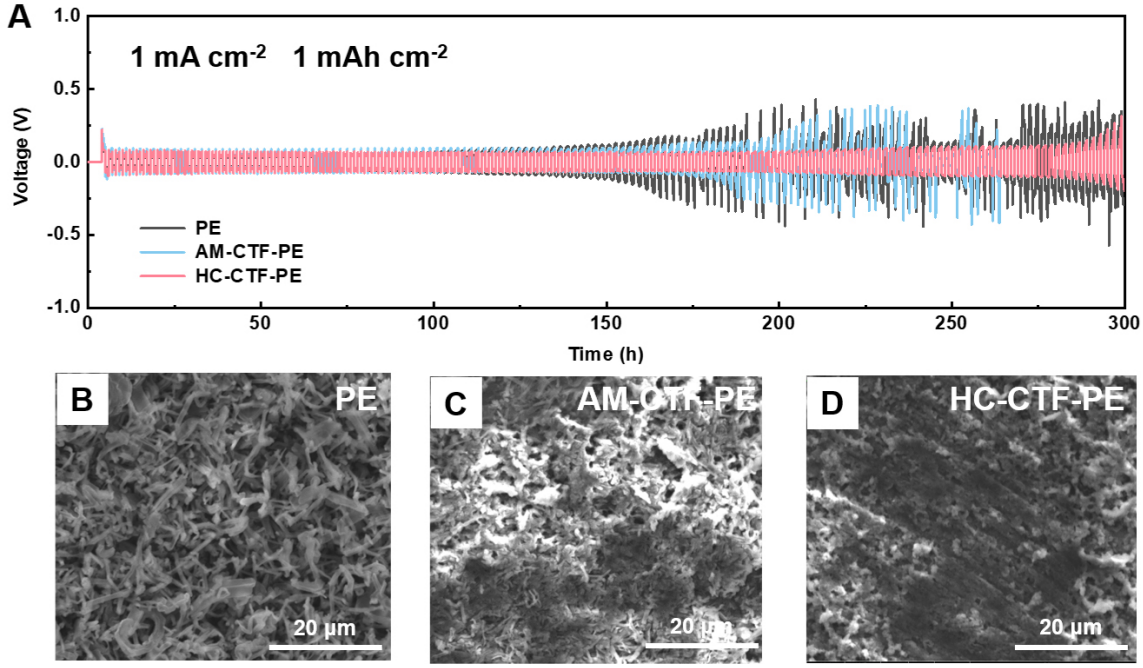

Figure 5. (A) Voltage-time profiles of Li//Li symmetric cells assembled with PE, AM-CTF-PE and HC-CTF-PE separators at 1 mA cm^{-2} with a capacity of 1 mAh cm^{-2}; SEM images of Cu electrodes from Cu//Li cells assembled with (B) PE, (C) AM-CTF-PE and (D) HC-CTF-PE separators after Li plating at a current density of 0.5 mA cm^{-2}.

obviously, abundant dendritic lithium grew on the Cu foil with the PE separator [Figure 5B]. Mossy dendrites are observed on the surface of the Cu foil with the AM-CTF-PE separator [Figure 5C]. When using the HC-CTF-PE separator, a much smoother Cu surface was obtained after cycling [Figure 5D]. Thus, due to the nanosized pores and desolvation effect, the HC-CTF-PE separator can regulate the ion flux and suppress the growth of dendritic lithium. And the electrochemical performance of the separators and assembled cells, including t_{Li^+}, ionic conductivity, and stability of lithium plating, are comparable with that in literature [Supplementary Table 4].

To further prove the prominent advantages of the HC-CTF-PE separator, the electrochemical performance of LFP//Li cells was investigated. The stability of the battery with different separators was evaluated by cycling performance tests. As shown in Figure 6A, the capacity of PE separator-assembled cells is only 23.4 mAh g^{-1} after 300 cycles at 1 C with the LFP loading of 1.58 mg cm^{-2}, which is considered as the poor cycling stability with a capacity retention rate of 16.8% of the first cycle capacity. Notably, the cells assembled with AM-CTF-PE and HC-CTF-PE separators exhibit excellent cycling stability, whose capacity retentions after 1,000 cycles maintain 41.8% and 45.4%, respectively. Meanwhile, in Figure 6B, the 100th circle discharge/charge voltage profiles at 1 C exhibit that the HC-CTF-PE separator has the lowest overpotential (0.17 V). However, the AM-CTF-PE and PE separators demonstrate relatively larger overpotential (0.25 and 0.43 V) and strong battery polarization. This may be induced by the irreversible loss of lithium metal and electrolyte. In addition, with increasing coating layer thicknesses, the pathway of ion transport across the separators is prolonged, resulting in the deterioration of battery performance [Supplementary Figure 13]. As shown in the following FT-IR spectra, the characteristic vibrations of the triazine units at 1,523 cm^{-1} (C=N) and 1,367 cm^{-1} (C-N) can clearly be observed in the separators after 100 cycles at 1 C of LFP/Li cells, suggesting the chemical stability of the CTF coatings [Supplementary Figure

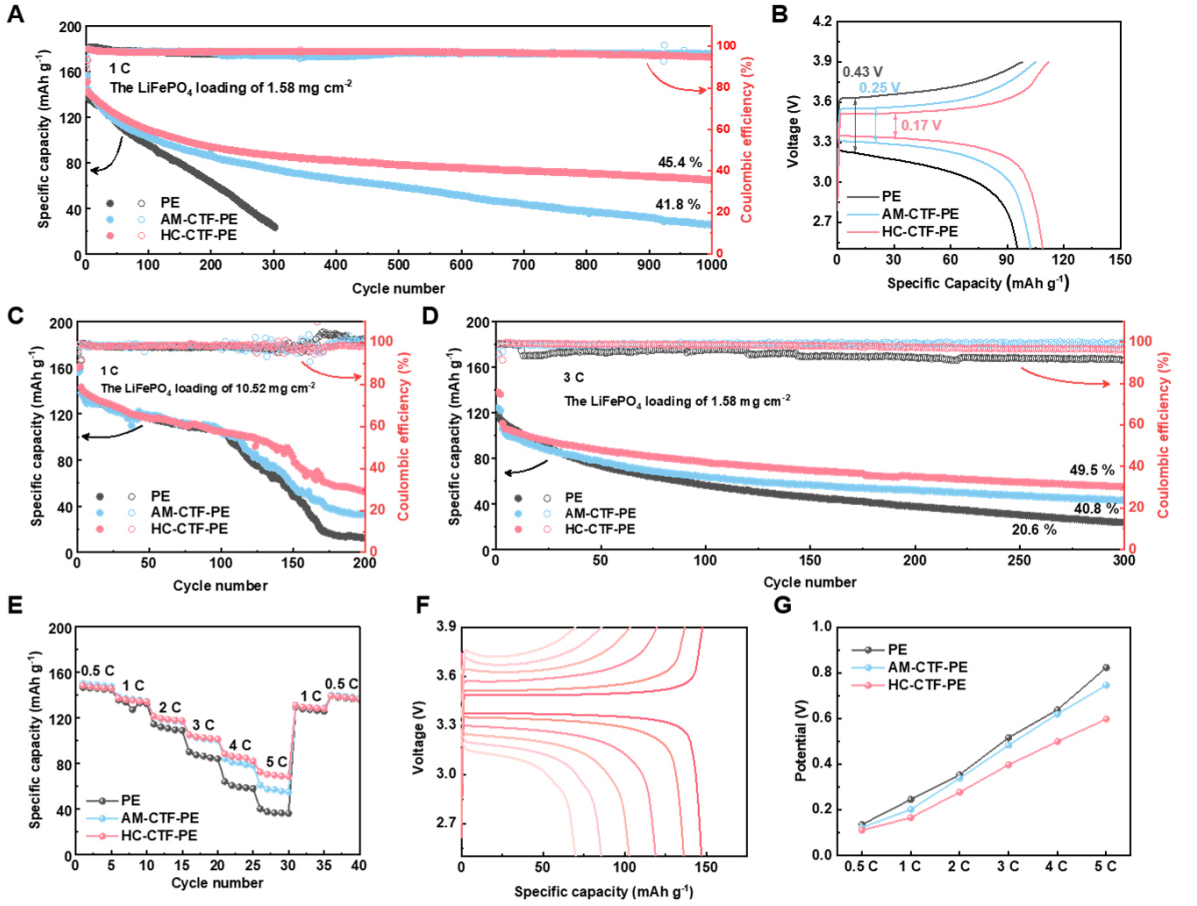

Figure 6. (A) Long-term cycling stability of LFP//Li cells at 1 C with the $LiFePO_4$ loading of 1.58 mg cm^{-2}; (B) Charge-discharge curves at 1 C for 100th revolution with the $LiFePO_4$ loading of 1.58 mg cm^{-2}; (C) Long-term cycling stability at 1 C with an increased $LiFePO_4$ loading of 10.52 mg cm^{-2}; (D) Cycling performance at 3 C with the $LiFePO_4$ loading of 1.58 mg cm^{-2}; (E) Rate performance of PE, AM-CTF-PE and HC-CTF-PE separators assembled cells at various current densities of 0.5-5 C; (F) Charge-discharge curves of HC-CTF-PE separator assembled cells at various current densities of 0.5-5 C; (G) The potential gaps of PE, AM-CTF-PE and HC-CTF-PE separators assembled cells at various rates, respectively.

14A]. In addition, from the EDS mapping of N elements of separators, their uniform dispersion indicates the structural integrity of CTF coating layers after cycling [Supplementary Figure 14B-E]. The surface morphology of CTF side of the cycled separators differs from the original ones due to deposited lithium during the cycling process. Further, to meet the requirements of practical application, higher LFP loading is necessary to increase the energy density of batteries. With commercial cathodes (LFP loading of 10.52 mg cm^{-2}), as shown in Figure 6C, the capacity of the HC-CTF-PE separator maintains 99.5 mAh g^{-1} after 120 cycles at 1 C, much higher than that of the AM-CTF-PE (85.22 mAh g^{-1}) and the PE (77.6 mAh g^{-1}).

To further prove the prominent advantages of the HC-CTF-PE separator, the electrochemical performance of LFP//Li cells was investigated. The stability of the battery with different separators was evaluated by cycling performance tests. As shown in Figure 6A, the capacity of PE separator-assembled cells is only 23.4 mAh g^{-1} after 300 cycles at 1 C with the LFP loading of 1.58 mg cm^{-2}, which is considered as the poor cycling stability with a capacity retention rate of 16.8% of the first cycle capacity. Notably, the cells assembled with AM-CTF-PE and HC-CTF-PE separators exhibit excellent cycling stability, whose capacity

retentions after 1,000 cycles maintain 41.8% and 45.4%, respectively. Meanwhile, in Figure 6B, the 100th circle discharge/charge voltage profiles at 1 C exhibit that the HC-CTF-PE separator has the lowest overpotential (0.17 V). However, the AM-CTF-PE and PE separators demonstrate relatively larger overpotential (0.25 and 0.43 V) and strong battery polarization. This may be induced by the irreversible loss of lithium metal and electrolyte. In addition, with increasing coating layer thicknesses, the pathway of ion transport across the separators is prolonged, resulting in the deterioration of battery performance [Supplementary Figure 13]. As shown in the following FT-IR spectra, the characteristic vibrations of the triazine units at 1,523 cm^{-1} (C=N) and 1,367 cm^{-1} (C-N) can clearly be observed in the separators after 100 cycles at 1 C of LFP/Li cells, suggesting the chemical stability of the CTF coatings [Supplementary Figure 14A]. In addition, from the EDS mapping of N elements of separators, their uniform dispersion indicates the structural integrity of CTF coating layers after cycling [Supplementary Figure 14B-E]. The surface morphology of CTF side of the cycled separators differs from the original ones due to deposited lithium during the cycling process. Further, to meet the requirements of practical application, higher LFP loading is necessary to increase the energy density of batteries. With commercial cathodes (LFP loading of 10.52 mg cm^{-2}), as shown in Figure 6C, the capacity of the HC-CTF-PE separator maintains 99.5 mAh g^{-1} after 120 cycles at 1 C, much higher than that of the AM-CTF-PE (85.22 mAh g^{-1}) and the PE (77.6 mAh g^{-1}).

The CE is further studied to evaluate the cell performance during repeated cycling. As shown in Figure 6D, the CEs of both HC-CTF-PE and AM-CTF-PE separators are around 95% over 300 cycles at 3 C. The HC-CTF-PE also has the highest capacity retention (49.5% after 300 cycles). However, the CE of PE separators is consistently unstable, with a low value of 90%. To clearly illustrate this trend, the enlarged graph of the CE for the first 100 cycles further shows the superior cycling stability of the HC-CTF separator [Supplementary Figure 15]. The lower and unstable CE of the pristine PE separator at 3 C suggests the Li^+ loss during each cycle. It is worth noting that the CE of the HC-CTF-PE separator-assembled cells slightly decreases after cycling. The decrease of the CE at the later stage of the battery may be due to soft short circuit inside the battery[50].

The rate performance of cells assembled with different separators was evaluated at current rates ranging from 0.5 to 5 C [Figure 6E]. The HC-CTF-PE separator can deliver the average specific capacity of 146, 136, 118, 102, 85 and 69 mAh g^{-1} at 0.5, 1, 2, 3, 4 and 5 C, respectively. By contrast, the AM-CTF-PE and PE separators show much lower capacities of 56 and 28 mAh g^{-1} at 5 C. It suggests a faster Li^+ transport kinetic in the HC-CTF-PE separator, especially at the high rate. The charge/discharge voltage curves of the corresponding HC-CTF-PE, AM-CTF-PE, and PE separators in Figure 6F, Supplementary Figures 16 and 17 clearly show that the CTF-coated separators have a clear discharge plateau, while the PE separator discharge platform contracts obviously. And the discharge capacity is significantly reduced due to the limited Li^+ transport rate of the PE separator. In addition, the HC-CTF-PE separator has the lowest overpotential at various charge and discharge rates [Figure 6G], indicating the weakest polarization and fastest Li^+ transport[51].

CONCLUSIONS

In summary, The AM-CTF and HC-CTF were successfully synthesized and coated on the surface of commercial PE separators. It can be found that compared with AM-CTF, the well-connected porous structure of HC-CTF shortens ion diffusion pathways, and a larger specific surface area provides more accessible active sites, enhancing ionic conductivity and t_{Li^+}. As a result, the Li//Li symmetric cells assembled with HC-CTF-PE separators exhibit excellent cycling stability for as long as 300 h with low polarization and negligible voltage fluctuation. The LFP/Li full cells based on HC-CTF-PE separators exhibit satisfying

lifespan, high-capacity retention (45.4% at 1 C for 1,000 cycles) and CE. Overall, this research offers a new strategy for improving the performance of COF-coated separators for high-energy-density lithium batteries.

DECLARATIONS

Acknowledgments

The authors acknowledge support from Shenzhen Senior Technology Material Co., Ltd. We also acknowledge access to SEM, FE-TEM, XRD and BET facilities of the Analytical and Testing Center of Huazhong University of Science and Technology.

Authors' contributions

Methodology, formal analysis, investigation, writing manuscript: Wang Y
Validation, resources, formal analysis: Chen Y, Wang X, Sun R, Yang Y
Methodology, visualization, investigation: Wang Y
Project administration, conceptualization, funding acquisition, supervision, writing manuscript: Nie H, Wang X, Tan B
Project administration, funding acquisition: Zhou X
Project administration, conceptualization, funding acquisition, supervision: Xie X

Availability of data and materials

The data supporting our work can be found in the Supplementary Materials.

Financial support and sponsorship

This work is supported by the Young Scientists Fund of the National Natural Science Foundation of China (52303084), Major International (Regional) Joint Cooperation Research Project of the National Natural Science Foundation of China (52020105012), the Young Scientists Fund of Natural Science Foundation of Hubei Province (2023AFB220), and the Open Research Fund (No. 2023JYBKF05) of Key Laboratory of Material Chemistry for Energy Conversion and Storage (HUST), Ministry of Education.

Conflicts of interest

All authors declare that there are no conflicts of interest.

Ethical approval and consent to participate

Not applicable.

Consent for publication

Not applicable.

REFERENCES

1. Li D, Hu H, Chen B, Lai WY. Advanced current collector materials for high-performance lithium metal anodes. *Small* 2022;18:e2200010. DOI
2. Zhang X, Chen X, Xu R, et al. Columnar lithium metal anodes. *Angew Chem* 2017;129:14395-9. DOI
3. Cheng XB, Zhang R, Zhao CZ, Wei F, Zhang JG, Zhang Q. A review of solid electrolyte interphases on lithium metal anode. *Adv Sci* 2016;3:1500213. DOI
4. Zhang K, Lee G, Park M, Li W, Kang Y. Recent developments of the lithium metal anode for rechargeable non-aqueous batteries. *Adv Energy Mater* 2016;6:1600811. DOI
5. Wang Q, Liu B, Shen Y, et al. Confronting the challenges in lithium anodes for lithium metal batteries. *Adv Sci* 2021;8:e2101111. DOI PubMed PMC

6. Liu K, Wang Z, Shi L, Jungsuttiwong S, Yuan S. Ionic liquids for high performance lithium metal batteries. *J Energy Chem* 2021;59:320-33. DOI
7. Li G. Regulating mass transport behavior for high-performance lithium metal batteries and fast-charging lithium-ion batteries. *Adv Energy Mater* 2021;11:2002891. DOI
8. Shen X, Liu H, Cheng X, Yan C, Huang J. Beyond lithium ion batteries: Higher energy density battery systems based on lithium metal anodes. *Energy Stor Mater* 2018;12:161-75. DOI
9. Li G, Liu Z, Huang Q, et al. Stable metal battery anodes enabled by polyethylenimine sponge hosts by way of electrokinetic effects. *Nat Energy* 2018;3:1076-83. DOI
10. Chen Y, Dou X, Wang K, Han Y. Lithium dendrites inhibition via diffusion enhancement. *Adv Energy Mater* 2019;9:1900019. DOI
11. Albertus P, Babinec S, Litzelman S, Newman A. Status and challenges in enabling the lithium metal electrode for high-energy and low-cost rechargeable batteries. *Nat Energy* 2018;3:16-21. DOI
12. Zhou P, Zhang X, Xiang Y, Liu K. Strategies to enhance Li^+ transference number in liquid electrolytes for better lithium batteries. *Nano Res* 2023;16:8055-71. DOI
13. Liang J, Chen Q, Liao X, et al. A nano-shield design for separators to resist dendrite formation in lithium-metal batteries. *Angew Chem* 2020;132:6623-8. DOI
14. Wang G, Xiong X, Xie D, et al. Suppressing dendrite growth by a functional electrolyte additive for robust Li metal anodes. *Energy Stor Mater* 2019;23:701-6. DOI
15. Din MMU, Murugan R. Metal coated polypropylene separator with enhanced surface wettability for high capacity lithium metal batteries. *Sci Rep* 2019;9:16795. DOI PubMed PMC
16. Wang C, Li W, Jin Y, Liu J, Wang H, Zhang Q. Functional separator enabled by covalent organic frameworks for high-performance Li metal batteries. *Small* 2023;19:e2300023. DOI
17. Chen H, Lin Q, Xu Q, Yang Y, Shao Z, Wang Y. Plasma activation and atomic layer deposition of TiO_2 on polypropylene membranes for improved performances of lithium-ion batteries. *J Membrane Sci* 2014;458:217-24. DOI
18. Wu J, Zeng H, Li X, et al. Ultralight layer-by-layer self-assembled MoS_2-polymer modified separator for simultaneously trapping polysulfides and suppressing lithium dendrites. *Adv Energy Mater* 2018;8:1802430. DOI
19. Naren T, Jiang R, Qing P, et al. Stabilizing lithium metal batteries by synergistic effect of high ionic transfer separator and lithium-boron composite material anode. *ACS Nano* 2023;17:20315-24. DOI
20. Zhang Y, Qiu Z, Wang Z, Yuan S. Functional polyethylene separator with impurity entrapment and faster Li^+ ions transfer for superior lithium-ion batteries. *J Colloid Interface Sci* 2022;607:742-51. DOI
21. Jin R, Fu L, Zhou H, et al. High Li^+ ionic flux separator enhancing cycling stability of lithium metal anode. *ACS Sustain Chem Eng* 2018;6:2961-8. DOI
22. Ding SY, Wang W. Covalent organic frameworks (COFs): from design to applications. *Chem Soc Rev* 2013;42:548-68. DOI PubMed
23. An Y, Tan S, Liu Y, et al. Designs and applications of multi-functional covalent organic frameworks in rechargeable batteries. *Energy Stor Mater* 2021;41:354-79. DOI
24. Zhou L, Jo S, Park M, et al. Structural engineering of covalent organic frameworks for rechargeable batteries. *Adv Energy Mater* 2021;11:2003054. DOI
25. Ye H, Zhang C, Li Y, et al. Advanced covalent-organic framework materials for sodium-ion battery. *Prog Nat Sci* 2023;33:754-66. DOI
26. Sun T, Xie J, Guo W, Li D, Zhang Q. Covalent-organic frameworks: advanced organic electrode materials for rechargeable batteries. *Adv Energy Mater* 2020;10:1904199. DOI
27. Chang H, Wu Y, Han X, Yi T. Recent developments in advanced anode materials for lithium-ion batteries. *Energy Mater* 2022;1:100003. DOI
28. Gao Z, Liu Q, Zhao G, Sun Y, Guo H. Covalent organic frameworks for solid-state electrolytes of lithium metal batteries. *J Mater Chem A* 2022;10:7497-516. DOI
29. Niu C, Luo W, Dai C, Yu C, Xu Y. High-voltage-tolerant covalent organic framework electrolyte with holistically oriented channels for solid-state lithium metal batteries with nickel-rich cathodes. *Angew Chem Int Ed* 2021;60:24915-23. DOI
30. Cao Y, Wang M, Wang H, Han C, Pan F, Sun J. Covalent organic framework for rechargeable batteries: mechanisms and properties of ionic conduction. *Adv Energy Mater* 2022;12:2200057. DOI
31. Cao Y, Wu H, Li G, et al. Ion selective covalent organic framework enabling enhanced electrochemical performance of lithium-sulfur batteries. *Nano Lett* 2021;21:2997-3006. DOI
32. Shi J, Tang W, Xiong B, Gao F, Lu Q. Molecular design and post-synthetic vulcanization on two-dimensional covalent organic framework@rGO hybrids towards high-performance sodium-ion battery cathode. *Chem Eng J* 2023;453:139607. DOI
33. Wang S, Wang Q, Shao P, et al. Exfoliation of covalent organic frameworks into few-layer redox-active nanosheets as cathode materials for lithium-ion batteries. *J Am Chem Soc* 2017;139:4258-61. DOI
34. Vadiyar MM, Kim J, Bae J, Nam K. Imidazole linker-induced covalent triazine framework-ZIF hybrids for confined hollow carbon super-heterostructures toward a long-life supercapacitor. *Carbon Energy* 2023;5:e344. DOI
35. Sun R, Tan B. Covalent triazine frameworks (CTFs): synthesis, crystallization, and photocatalytic water splitting. *Chemistry* 2023;29:e202203077. DOI PubMed
36. Liu M, Guo L, Jin S, Tan B. Covalent triazine frameworks: synthesis and applications. *J Mater Chem A* 2019;7:5153-72. DOI

37. Zhang Y, Jin S. Recent advancements in the synthesis of covalent triazine frameworks for energy and environmental applications. *Polymers* 2018;11:31. DOI PubMed PMC
38. Wang K, Yang LM, Wang X, et al. Covalent triazine frameworks via a low-temperature polycondensation approach. *Angew Chem Int Ed* 2017;56:14149-53. DOI PubMed PMC
39. Liu M, Jiang K, Ding X, et al. Controlling monomer feeding rate to achieve highly crystalline covalent triazine frameworks. *Adv Mater* 2019;31:e1807865. DOI
40. Evans J, Vincent CA, Bruce PG. Electrochemical measurement of transference numbers in polymer electrolytes. *Polymer* 1987;28:2324-8. DOI
41. Chen Y, Mickel P, Pei H, et al. Bioinspired separator with ion-selective nanochannels for lithium metal batteries. *ACS Appl Mater Interfaces* 2023;15:18333-42. DOI
42. Guo Y, Niu P, Liu Y, et al. An Autotransferable g-C_3N_4 Li^+-modulating layer toward stable lithium anodes. *Adv Mater* 2019;31:e1900342. DOI
43. Zhang R, Chen XR, Chen X, et al. Lithiophilic sites in doped graphene guide uniform lithium nucleation for dendrite-free lithium metal anodes. *Angew Chem Int Ed* 2017;56:7764-8. DOI
44. Zhou T, Zhao Y, Choi JW, Coskun A. Lithium-salt mediated synthesis of a covalent triazine framework for highly stable lithium metal batteries. *Angew Chem* 2019;131:16951-5. DOI PubMed
45. Bai P, Li J, Brushett FR, Bazant MZ. Transition of lithium growth mechanisms in liquid electrolytes. *Energy Environ Sci* 2016;9:3221-9. DOI
46. Sand HJ. III. On the concentration at the electrodes in a solution, with special reference to the liberation of hydrogen by electrolysis of a mixture of copper sulphate and sulphuric acid. *Lond Edinb Dublin Philos Mag J Sci* 1901;1:45-79. DOI
47. Kim D, Liu X, Yu B, et al. Amine-functionalized boron nitride nanosheets: a new functional additive for robust, flexible ion gel electrolyte with high lithium-ion transference number. *Adv Funct Mater* 2020;30:1910813. DOI
48. Li L, Wang M, Wang J, et al. Asymmetric gel polymer electrolyte with high lithium ion conductivity for dendrite-free lithium metal batteries. *J Mater Chem A* 2020;8:8033-40. DOI
49. Ghazi ZA, Sun Z, Sun C, et al. Key aspects of lithium metal anodes for lithium metal batteries. *Small* 2019;15:e1900687. DOI
50. Xiao J, Li Q, Bi Y, et al. Understanding and applying coulombic efficiency in lithium metal batteries. *Nat Energy* 2020;5:561-8. DOI
51. Zhang C, Shen L, Shen J, et al. Anion-sorbent composite separators for high-rate lithium-ion batteries. *Adv Mater* 2019;31:e1808338. DOI